npj | Computational Materials

www.nature.com/npjcompumats

Corrected: Author correction

ARTICLE OPEN

Strain engineering of electro-optic constants in ferroelectric materials

Charles Paillard[1], Sergei Prokhorenko[1] and Laurent Bellaiche[1]

Electro-optic effects allow control of the ow of light using electric fields, and are of utmost importance for today's information and communication technologies, such as TV displays and fiber optics. The search for large electro-optic constants in films is essential to the miniaturization and increased efficiency of electro-optic devices. In this work, we demonstrate that strain-engineering in $PbTiO_3$ films allows to selectively choose which electro-optic constant to improve. Unclamped electro-optic constants larger than 100 pm V^{-1} are predicted, either by driving the softening of an optical phonon mode at a phase transition boundary under tensile strain, or by generating the equivalent of a negative pressure via compressive strain to obtain large piezoelectric constants. In particular, a r_{13} electro-optic coefficient twice as large as the one of the commonly used $LiNbO_3$ electro-optic material is found here when growing $PbTiO_3$ on the technologicallyimportant Si substrate.

npj Computational Materials (2019)5:6 ; https://doi.org/10.1038/s41524-018-0141-4

INTRODUCTION

The control of the propagation of light with electric fields is of paramount importance in information and computing technologies. Those electro-optic (EO) effects are used in display technologies,[1,2] waveguide modulators,[3] or tunable microring resonators,[4] and are key to the development and optimization of optoelectronic devices[5]. Nowadays, technologies rely primarily on a modulation of the refractive index of a material which depends either linearly[6] (linear EO or Pockels effect) or quadratically (quadratic EO/Kerr effect[7,8]) on the applied electric field. There is thus a growing demand to find EO materials with EO constants superseding the standard 32.2 pm V^{-1} in $LiNbO_3$.[9] Our calculations show that the proximity of phase transitions or the use of an original negative-like pressure effect[10] may lead to EO constants larger than 100 pm V^{-1} in ferroelectric films.

Interestingly, it appears that the EO constants are reduced by one order of magnitude, when $BaTiO_3$ is deposited in thin films[11,12]—which may be due to extrinsic effects. To improve the efficiency and miniaturization of EO devices, it is therefore important to discover and understand general mechanisms that can intrinsically enhance (rather than suppress) the EO constants in films. This work focuses on the EO properties of strained lead titanate. $PbTiO_3$ is a classical ferroelectric that is a member of a wide range of materials (such as $Pb_{1-x}La_xZr_{1-y}Ti_yO_3$ or PLZT) which are known to exhibit large piezoelectric constants and have been under scrutiny to get large EO constants.[13,14] Using accurate ab initio techniques,[9,15] we explore a wide range of epitaxial strain conditions and identify general mechanisms resulting in large EO effects in ferroelectric $PbTiO_3$ films.

After describing the structure of $PbTiO_3$ under strain, we discuss below the clamped EO constants and link their large values under tensile strain with lattice instabilities at phase boundaries. Finally, we investigate the unclamped EO constants and further explain the origins of their large magnitude for some particular compressive strains—including the one induced by the technologically important Si substrate.

RESULTS

$PbTiO_3$ under strain

Using the ABINIT code,[16] we calculated the relaxed structures of $PbTiO_3$ under strain using a 20-atom supercell (see Fig. 1b) to accommodate the monoclinic and orthorhombic phases existing under tensile strain.[17] The supercell is rotated by $\pi/4$ radians with respect to the Cartesian axes $\boldsymbol{a}_1$, $\boldsymbol{a}_2$, and $\boldsymbol{a}_3$ (see Supplementary Material). As depicted in Fig. 1b, the Cartesian axes exactly coincide with the pseudocubic axes of the 5-atom unit cell of the *P*4*mm* ground state of bulk $PbTiO_3$. We shall refer to those Cartesian axes as the "lab axes". All tensor quantities are expressed in this basis. The in-plane lattice vectors of the supercell are kept fixed and their length imposed to generate a bi-axial strain, and the third vector is allowed to relax.

As observed in Fig. 1a, the energy of the tetragonal *P*4*mm* phase, with polarization along the tetragonal axis [001] in the pseudocubic axes, is the lowest under compressive strain and up to tensile strain of 0.8%—consistent with the fact that *P*4*mm* is the ground state of bulk $PbTiO_3$. Beyond, and up to ≈1.3% tensile strain, a monoclinic *Cm* phase bridges the tetragonal phase with an orthorhombic *Ic*2*m* phase at larger tensile strain, in qualitative agreement with ref. [17] and the phenomenological work of ref. [18]. This orthorhombic phase has a polarization along a ⟨110⟩ pseudocubic direction.

We already note that the *c*/*a* ratio of the tetragonal phase shows a sharp increase at large compressive strain $\eta \simeq -2.5\%$ in Fig. 1c, which is reminiscent of the anomalous enhancement of tetragonality found in $PbTiO_3$ under negative pressure.[10] As a result of this effect, the piezoelectric constant d_{33} exhibits a large increase up to 80 p C N^{-1} within the tetragonal phase, as also displayed in Fig. 1d.

[1]Department of Physics and Institute for Nanoscience and Engineering, University of Arkansas, Fayetteville, AR 72701, USA
Correspondence: Laurent Bellaiche (laurent@uark.edu)

Received: 13 August 2018 Accepted: 6 December 2018
Published online: 08 January 2019

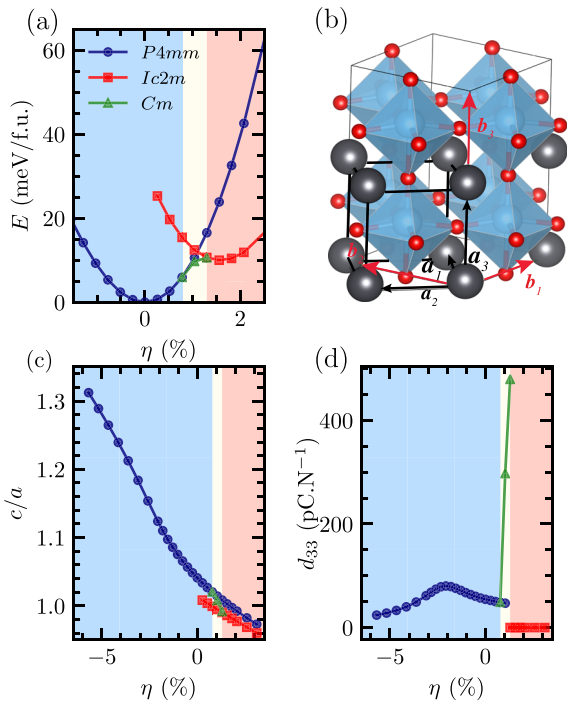

Fig. 1 **a** Energy of the tetragonal, monoclinic, and orthorhombic phases with respect to strain. **b** Sketch of the 5-atom unit cell and the Cartesian axes $\boldsymbol{a}_1$, $\boldsymbol{a}_2$, and $\boldsymbol{a}_3$, as well as the 20-atom supercell and its axes $\boldsymbol{b}_1$, $\boldsymbol{b}_2$, and $\boldsymbol{b}_3$. **c** c/a ratio in the tetragonal, monoclinic, and orthorhombic supercell. **d** Calculated piezoelectric constant d_{33} in the three considered phases. Data indicated in blue circles, green triangles, and red squares correspond to tetragonal, monoclinic, and orthorhombic phases, respectively, in (**a**, **c**, **d**)

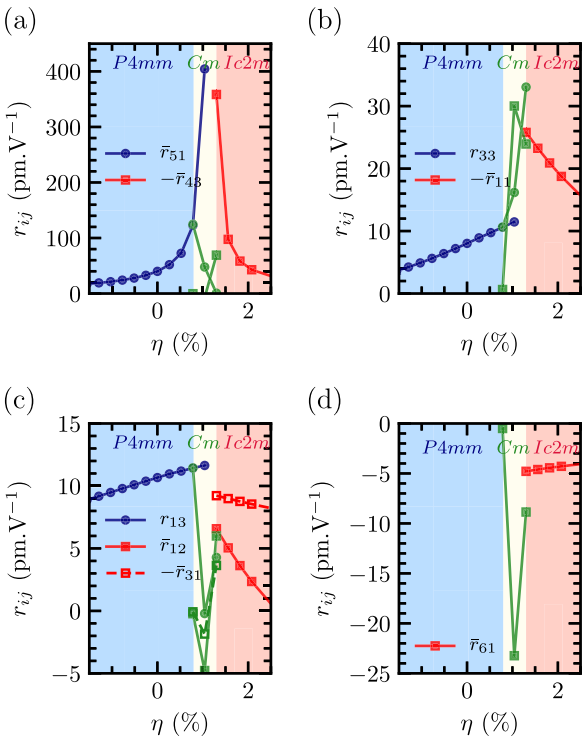

Fig. 2 Evolution of the clamped EO constants with strain η. Symbols indicate the EO constant under consideration (e.g., circles for r_{51} in (**a**)) while the color indicate the phase, that is tetragonal (blue), monoclinic (green), or orthorombic (red)

Clamped EO constants

The linear EO constants r_{ijk} describe the first-order dependence of the inverse of the optical dielectric constant ε_{ij} (approximated by the electronic dielectric constant) when a static or low-frequency electric field $\boldsymbol{E}$ is applied,

$$\Delta\left(\varepsilon^{-1}\right)_{ij} = \sum_{k=1}^{3} r_{ijk} E_k. \tag{1}$$

The *clamped* EO constants r_{ijk}^{η} can be decomposed into (i) a purely electronic term which depends on the second-order dielectric susceptibility $\chi_{ijk}^{(2)}$, and (ii) a phonon-induced change of the optical dielectric susceptibility which can be expressed in terms of the Raman susceptibility a_{ij}^{m} and polarity p_i^m of a transverse optical (TO) mode of frequency ω_m:[9,15,19]

$$r_{ijk}^{\eta} = \frac{-8\pi}{n_i^2 n_j^2} \chi_{ijk}^{(2)} - \frac{4\pi}{n_i^2 n_j^2 \sqrt{V_0}} \sum_m \frac{a_{ij}^m p_k^m}{\omega_m^2}, \tag{2}$$

with n_i being a principal refractive index and V_0 is the cell volume. All quantities of Eq. (2) can be calculated by density functional perturbation theory (DFPT).[15]

We give the clamped EO constants for the different phases in Fig. 2, expressed in the Cartesian basis $\boldsymbol{a}_1$, $\boldsymbol{a}_2$, and $\boldsymbol{a}_3$—which corresponds to the pseudocubic axes in the *P4mm* phase. We note, using the Voigt notation for the first two indices, that only the components $r_{42} = r_{51}$, r_{33}, and $r_{13} = r_{23}$ are nonzero in the *P4mm* phase, each of which are denoted by blue circle in Fig. 2a–c, respectively. For the bulk clamped EO constants (corresponding to zero strain), we obtain $r_{51} = 40.0$ pm V^{-1}, $r_{33} = 8.0$ pm V^{-1}, and $r_{13} = 10.7$ pm V^{-1}, consistent with the values in ref. [9], which were computed using the experimental structure. At the boundary between the *P4mm* and *Cm* phases ($\eta \approx 0.8\%$), the average $\bar{r}_{51} = \frac{r_{42}+r_{51}}{2}$ is ≈122.9 pm V^{-1}, that is three times as large as the bulk value! r_{33} and r_{13} are also moderately increased with respect to their corresponding bulk values, by 32% and 7%, respectively, near this boundary.

In the orthorhombic phase *Ic2m*, in the lab axes, the only nonzero components of the EO tensor are $r_{11} = r_{22}$, $r_{12} = r_{21}$, $r_{31} = r_{32}$, $r_{43} = r_{53}$, and $r_{61} = r_{62}$, and are depicted in Fig. 2 too. r_{43} strongly diverges when approaching the phase transition toward the *Cm* phase. Right before the boundary, a value of $r_{43} = -100$ pm V^{-1} is predicted at a strain of 1.6%, while at $\eta \approx 1.3\%$, the *Cm* phase is slightly more favorable energetically, and the EO constant r_{43} drops in magnitude to -24 pm V^{-1}. By comparison, in the metastable orthorhombic phase at this latter strain, r_{43} is as large as -351 pm V^{-1}. The in-plane EO constants r_{11} and r_{22}, which are associated with directions having nonzero components of the polarization, are rather large at such strain too. They are ≈-23 pm V^{-1}, which is about the magnitude of the room-temperature value of $LiNbO_3$ in the polar-axis direction (≈30 pm V^{-1}[19,20]).

The *Cm* phase structurally bridges the *P4mm* and orthorhombic phases, which has an effect on EO coefficients. In particular, the diverging r_{51} and r_{43} EO constants smoothly vanish from each side of the *P4mm*–*Cm* and *Cm*–*Ic2m* transition, respectively; the diagonal EO constants r_{33} and $-r_{11}$ are enhanced in the *Cm* state, reaching values beyond 30 pm V^{-1}. Similarly, there is a strong increase of the $-r_{61}$ constant in the middle of the stability window of the *Cm* phase (see Fig. 2d)

Enhanced EO effect by lattice instabilities

To understand the origin of the strong divergence of the EO constants at phase boundaries in Fig. 2, we performed a DFPT calculation of the phonon spectrum at the Γ point of our supercell in the tetragonal phase. Because we use a 20-atom supercell, we

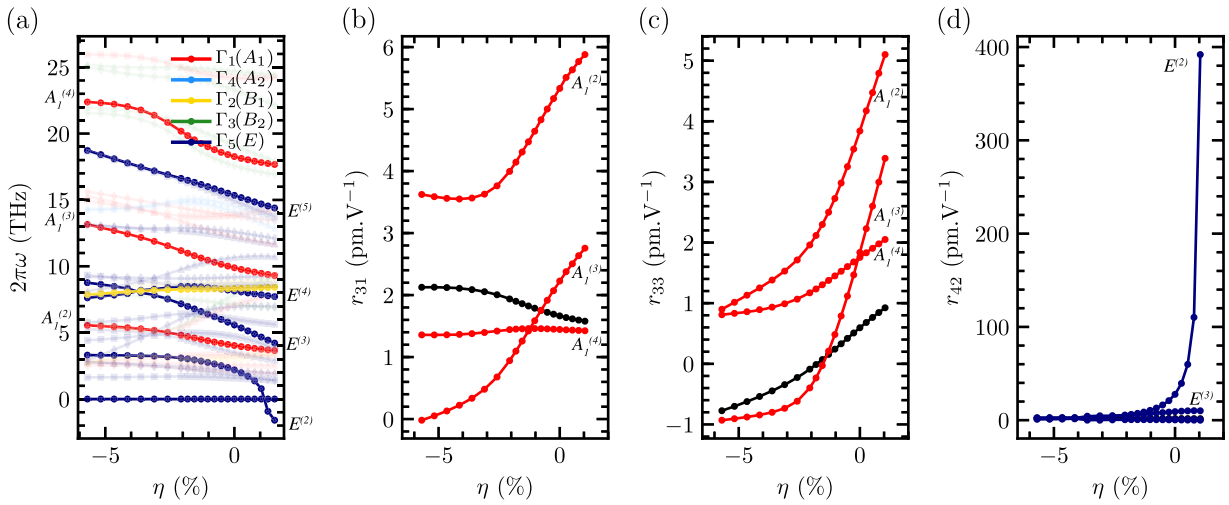

Fig. 3 **a** Evolution of phonon frequencies at Γ in the 20-atom supercell in the *P*4*mm* phase; the true Γ phonons of the 5-atom unit cell are presented with solid line and circles, while phonons corresponding to the *M*, *Z*, and *A* points in the 5-atom unit cell are plotted as semitransparent lines. The optical mode contributing to the EO constants r_{33} and r_{13} are denoted as $A_1^{(2)}$, $A_1^{(3)}$, and $A_1^{(4)}$, while the modes $E^{(2)}$, $E^{(3)}$, $E^{(4)}$, and $E^{(5)}$ contribute to r_{51}. **b** Mode decomposition of the EO constant r_{13}. Red lines correspond to modes of A_1 symmetry, while the black line depicts the electronic contribution. **c** Mode decomposition of the EO constant r_{33}. Red lines correspond to modes of A_1 symmetry, while the black line displays the electronic contribution. **d** Mode decomposition of the EO constant $r_{42} = r_{51}$. Blue lines correspond to modes of *E* symmetry, while the black line shows the electronic contribution

also actually obtain phonons from the $Z = (0, 0, 1/2)$, $M = (1/2, 1/2, 0)$ and $A = (1/2, 1/2, 1/2)$ points in the first Brillouin zone, whose frequency evolution with strain are plotted as semitransparent lines in Fig. 3a. Those points cannot couple with long-wavelength light, and thus do not contribute to the linear EO effect. In addition, the frequency evolution of the TO phonon modes at Γ are plotted as solid lines in Fig. 3a, according to the relevant symmetry of each mode. The lattice vibrations at the Γ point are made of four modes transforming as the irreducible representation A_1, one mode of symmetry B_1 and five doubly degenerate modes of symmetry *E*.[21] Because a mode must be Raman active and infrared (IR) active to contribute to the EO effect (see Eq. (2)), and given the symmetry of the Raman tensor and the IR selection rules in the *P*4*mm*, only the modes of symmetry A_1 (red modes in Fig. 3a) should contribute to r_{33} and r_{13}, which is indeed seen in Fig. 3b, c. Similarly, the *E* modes (blue modes) contributes only to $r_{51} = r_{42}$ (see Fig. 3d), while the mode B_1 does not contribute to EO constants.

Interestingly, we observe in Fig. 3d that most of the divergence of r_{51} is carried by a single optical *E* mode, denoted as $E^{(2)}$. This mode is the *E* mode that softens under tensile strain and whose frequency becomes imaginary at $\eta \approx 1.2\%$ in Fig. 3a, as consistent with the ω_m^{-2} dependency of a phonon contribution to the EO constant of Eq. (2). The divergence observed in the tetragonal phase of $PbTiO_3$ most likely explains the giant value of r_{42} observed in tetragonal $BaTiO_3$ bulk at room temperature,[22] as the proximity of the transition to an orthorhombic phase causes an *E* mode to soften.[23] In $BaTiO_3$ bulk, this softening is temperature driven, while in $PbTiO_3$ films it is strain-driven but similarly results in the divergence of $r_{42} = r_{51}$. We note that the temperature softening in $BaTiO_3$ most likely allows to keep large effective EO constants in thin-film form[24] (≈150 pm V^{-1}), and thus a clever phase transition engineering using both strain and temperature may result in giant EO constants.

One can also note a small softening of the A_1 modes near the *P*4*mm*-to-*Cm* transition, causing r_{13} and r_{33} to increase, albeit not in the same proportions as r_{51}. In the orthorhombic phase, the large value of r_{43} depicted in Fig. 2a is also the consequence of a single mode that softens near $\eta = 1.2\%$ (see Supplementary Material).

Unclamped EO constants

In many cases, *unclamped* (or stress free) EO constants r_{ijk}^{σ} rather than the clamped (strain free) ones r_{ijk}^{η} are more relevant to technologies. Those two sets of EO constants are related by the elasto-optic constants p_{ijkl} and the piezoelectric constants d_{ijk},[25]

$$r_{ijk}^{\sigma} = r_{ijk}^{\eta} + \sum_{m,n} p_{imn} d_{mnk}. \quad (3)$$

In the case of a (001)-oriented film, we are not dealing with fully unclamped EO constants, but rather only partially unclamped in the third direction, i.e., $r_{ijk}^{\eta_1\eta_2\sigma_3\sigma_4\sigma_5\eta_6}$; in other words, the material is free to deform its out-of-plane length (stress free along the third direction, hence the σ_3 superscript) and angles (hence the σ_4 and σ_5 superscripts), but the lengths and angle of the in-plane lattice vector are fixed (hence the superscripts η_1, η_2, and η_6). Only a handful of elasto-optic constants (namely, pi_3, pi_4, and pi_5) and piezoelectric constants (i.e., d_{3k}, d_{4k}, and d_{5k}) are thus needed. Their calculation is given in the Supplementary Material, and the partially unclamped EO constants are shown in Fig. 4.

The contribution of the elasto-optic and piezoelectric effects do not affect significantly the r_{51} or r_{43} unclamped EO constants in the *P*4*mm* and *Ic*2*m* phases, respectively, since the elasto-optic constant p_{55} and p_{44}, which couple to the diverging piezoelectric constants d_{51} and d_{43}, are small (see Supplementary Material). On the other hand, the p_{33} and p_{31} elasto-optic constants in the *P*4*mm* phase are rather strong (see Supplementary Material), and the large increase of the d_{33} piezoelectric constant at $\eta = -2.5\%$ (see Fig. 1d) induces a plateau in r_{33} and a local maximum in r_{13} at 24.1 pm V^{-1}. More interestingly, owing to the phase-transition induced divergence of d_{33} in the monoclinic phase, the unclamped EO constant r_{33} reaches as high as 124 pm V^{-1}, which is roughly four times its clamped value and represent a four time increase with respect to the zero strain value of the unclamped EO constant in the tetragonal phase (for which r_{33} approximate equals to 30.5 pm V^{-1}).

DISCUSSION

Two different paths to design large EO constants in ferroelectric $PbTiO_3$ films are demonstrated here. Firstly, the strain-induced

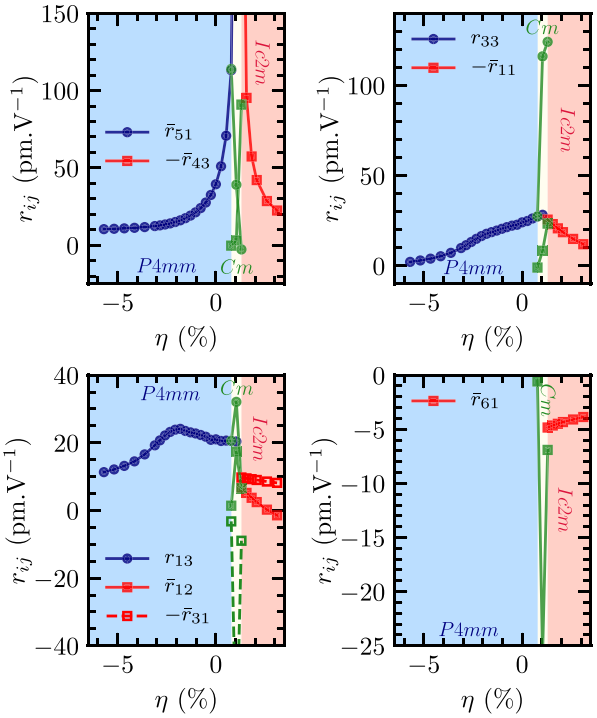

Fig. 4 Partially unclamped EO constants for a thin-film geometry. The symbol represents the EO constant under consideration (e.g., circle for r_{51} in **a**) while the color represents the phase (namely, blue for *P4mm*, green for *Cm* and red for *Ic2m*)

softening of a TO mode under tensile strain generates large contribution to the relevant EO constants. In this specific case, at the *P4mm–Cm* phase transition, the destabilization of an *E* mode of the *P4mm* phase leads to an extremely large response of the r_{51} constant; similarly, at the *Ic2m–Cm* phase boundary, r_{43} is large, while it vanishes in the *P4mm* phase. Such a mechanism has also been demonstrated for temperature-driven mode softening, typically in the tetragonal phase of $BaTiO_3$ bulk. In both $PbTiO_3$ films and $BaTiO_3$ bulk, the large increase of the clamped r_{51} near the tetragonal-orthorhombic phase transition can be traced back to the divergence of the dielectric constant.[26,27] The unclamped r_{51} in $BaTiO_3$ bulk also receives a significant contribution from the combined elasto-optic and piezoelectric effect.[28] On the other hand, in tetragonal $PbTiO_3$ film close to the *P4mm–Cm* transition, the elasto-optic constant p_{55} is too small, and despite the divergence of d_{51} driven by the soft mode, the unclamped r_{51} EO constant is not significantly further affected. The difference between unclamped and clamped EO constant is mainly mechanical (low-frequency) in nature through the piezoelectric effect. In PTO, that difference is small near the *P4mm–Cm* transition for the in-plane EO constants. Hence, PTO becomes particularly interesting, as a broad range of frequencies for the applied external electric field can be used without significantly affecting the EO constants in this strain region.

On the other hand, at the *Cm–Ic2m* phase boundary, large out-of-plane EO constants (r_{33} 124 pm V^{-1}) can be engineered due to the strain-induced divergence of the piezoelectric constant d_{33}. The latter comes from the flattening of the energy landscape to allow for polarization rotation from the [001] pseudo-cubic direction to [110] pseudo-cubic direction[19,20]. We thus show that strain, through the exploration of phases with different symmetries, allows tuning of the EO constants within a single material.

On the other hand, the anomalous behaviors of unclamped r_{33} and r_{13} of $PbTiO_3$ films obtained under the compressive strain η close to −2.5% are much more intriguing. They do not come from any phonon mode, nor from the electronic contribution, as no large clamped EO constant is observed around that strain (see Fig. 3b, c). Rather, they come from the strong peak in the piezoelectric constant d_{33} seen in Fig. 1d and thus represent an original way to change EO constants, that is by using electromechanical effects only. The extremely large enhancement of the piezoelectric constant at −2.5% compressive strain is associated with the strong increase in tetragonality *c*/*a* observed in Fig. 1c. The latter is reminiscent of the behavior of $PbTiO_3$ under negative pressure.[10] Note that increase of the piezoelectric constants under negative pressure has been confirmed experimentally in $PbTiO_3$ nanowires recently.[29] The origin of this piezoelectric enhancement was attributed to the proximity of a first-order phase transition in the energy landscape.[10] It gives another route to design large EO constants in ferroelectric oxide thin films by mimicking "negative pressure" effects with strain, and can potentially be achieved in $PbTiO_3$ films grown on the common $LaAlO_3$ substrate, that should provide a strain close to −2.9%.

Overall, $PbTiO_3$ (and related compounds) in film forms thus represent an interesting alternative to $LiNbO_3$ for obtaining various large EO components, since one can selectively improve different EO constants by working either with tensile or compressive strain. In addition, we note that, at room temperature, the strain of epitaxially grown (001)-$PbTiO_3$ films on silicon (which will constitute an essential step toward the realization of miniaturized integrated EO devices), should be close to −1.6%, assuming a 45° epitaxy.[30,31] At such strain, Fig. 4c reveals that the unclamped EO constant r_{13} is ≈23.4 pm V^{-1}, which is already more than twice as much as that of the standard EO material, $LiNbO_3$!

There are still technical issues that remain to be addressed from an experimental point of view. First of all, growth of perovskite oxides on Si is not straightforward, and often one resorts to the use of buffer layers such as $SrTiO_3$, that can partially relax the strain, in the case of $BaTiO_3$/Si for instance.[11] Other parameters, such as defects, or thermal expansion mismatch may relax part of the strain induced by the sole lattice mismatch (as considered in this work). Domain engineering, understanding the impact of the inhomogeneity of strain, applied electric fields, and dielectric losses near phase transitions are also necessary steps towards the design of efficient EO devices.

The two paths mentioned in this discussion section, as well as their elucidated mechanisms, can nonetheless serve as guiding principles to experimentally or computationally (via, e.g., machine learning techniques) discover various materials exhibiting large EO responses.

METHODS

We used the ABINIT[16] plane-wave code with norm-conserved pseudopotentials containing 14, 12, and 6 valence electrons for Pb, Ti, and O, respectively. We employed the nonspin-polarized local density approximation and a 50 Ha plane-wave cut-off. The structural relaxation was performed with a 4 × 4 × 3 *k*-mesh in the 20-atom supercell, and is achieved when the force on any ion is smaller than 5×10^{-5} Ha Bohr^{-1}. The electronic density was considered converged when forces between two self-consistent fields iterations are smaller than 10^{-6} Ha Bohr^{-1}. DFPT calculations of the EO constants are based on the linear variation of the electronic dielectric tensor when the system is perturbed by a low-frequency/static applied electric field.[9,15] As such, the calculated EO constants are dispersionless, and are valid in the limit when the wavelength of the incoming light is much larger than the absorption edge. The bandgap of lead titanate being around 3.4–3.9 eV,[32,33] this holds for most visible and Infrared wavelengths. For DFPT calculations of the EO constants, the same plane-wave cut-off was used, but the *k*-mesh was densified to 7 × 7 × 5.

DATA AVAILABILITY

Correspondence and request for material should be addressed to paillard@uark.edu.

ACKNOWLEDGMENTS

We thank Dr. A. Urbas for useful discussions. C.P. thanks the AHPCC for use of computing ressources. C.P. and L.B. thank the ARO grant W911NF-16-1-0227. S.P. and L.B. acknowledge DARPA grant HR0011-15-2-0038 (MATRIX program).

AUTHOR CONTRIBUTIONS

L. B. suggested and oversaw the study. C. P. and S. P. ran simulations. C. P. and L. B. analyzed the data and discussed them with S. P.; C. P., S. P., and L. B. wrote the manuscript.

ADDITIONAL INFORMATION

Supplementary information accompanies the paper on the *npj Computational Materials* website (https://doi.org/10.1038/s41524-018-0141-4).

Competing interests: The authors declare no competing interests.

Publisher's note Springer Nature remains neutral with regard to jurisdictional claims in published maps and institutional affiliations.

REFERENCES

1. Uchino, K. Electro-optic ceramics and their display applications. *Ceram. Int.* **21**, 309–315 (1995).
2. Uchino, K. *Ferroelectric Devices* (CRC Press, Boca Raton, USA 2009).
3. Xu, Q., Schmidt, B., Pradhan, S. & Lipson, M. Micrometre-scale silicon electro-optic modulator. *Nature* **435**, 325–327 (2005).
4. Guarino, A., Poberaj, G., Rezzonico, D., Degl'Innocenti, R. & Günter, P. Electro-optically tunable microring resonators in lithium niobate. *Nat. Photonics* **1**, 407–410 (2007).
5. Sando, D., Yang, Y., Paillard, C., Dkhil, B., Bellaiche, L. & Nagarajan, V. Epitaxial ferroelectric oxide thin films for optical applications. *Applied Physics Reviews* **5**, 041108 (2018).
6. Saleh, B. E. A. & Teich, M. C. *Fundamentals of Photonics*. (Wiley, New-York, 1991).
7. Kerr, J. XL A new relation between electricity and light: dielectrified media birefringent. *Philos. Mag. J. Sci.* **50**, 337–348 (1875).
8. Kerr, J. LIV A new relation between electricity and light: dielectrified media birefringent. *Philos. Mag. J. Sci.* **50**, 446–458 (1875).
9. Veithen, M., Gonze, X. & Ghosez, P. First-principles study of the electro-optic effect in ferroelectric oxides. *Phys. Rev. Lett.* **93**, 187401 (2004).
10. Tinte, S., Rabe, K. M. & Vanderbilt, D. Anomalous enhancement of tetragonality in $PbTiO_3$ induced by negative pressure. *Phys. Rev. B* **68**, 144105 (2003).
11. Abel, S. et al. A strong electro-optically active lead-free ferroelectric integrated on silicon. *Nat. Commun.* **4**, 1671 (2013).
12. Kormondy, K. et al. *Microelec. Eng.* **147**, 215–218 (2015).
13. Yi, G., Wu, Z. & Sayer, M. Preparation of $Pb(Zr,Ti)O_3$ thin films by sol gel processing: electrical, optical, and electro-optic properties. *J. Appl. Phys.* **64**, 2717–2724 (1988).
14. Takeda, K., Hoshina, T., Takeda, H. & Tsurumi, T. Electro-optic effect and photoelastic effect of ferroelectric relaxors. *Jpn. J. Appl. Phys.* **55**, 10TB05 (2016).
15. Veithen, M., Gonze, X. & Ghosez, P. Nonlinear optical susceptibilities, Raman efficiencies, and electro-optic tensors from first-principles density functional perturbation theory. *Phys. Rev. B* **71**, 125107 (2005).
16. Gonze, X. et al. ABINIT: first-principles approach to material and nanosystem properties. *Comput. Phys. Commun.* **180**, 2582–2615 (2009).
17. Chen, L. et al. Large elasto-optic effect in epitaxial $PbTiO_3$. *Phys. Rev. Lett.* **115**, 267602 (2015).
18. Pertsev, N. A., Zembilgotov, A. G. & Tagantsev, A. K. Equilibrium states and phase transitions in epitaxial ferroelectric thin films. *Ferroelectrics* **223**, 79–90 (1999).
19. Kaminow, I. P. & Johnston, W. D. Jr Quantitative determination of sources of the electro-optic effect in $LiNbO_3$. *Phys. Rev.* **160**, 519–522 (1967).
20. Turner, E. H. High-frequency electro-optic coefficients of lithium niobate. *Appl. Phys. Lett.* **8**, 303–304 (1966).
21. García, A. & Vanderbilt, D. First-principles study of stability and vibrational properties of tetragonal $PbTiO_3$. *Phys. Rev. B* **54**, 3817–3824 (1996).
22. Zgonik, M. et al. Dielectric, elastic, piezoelectric, electro-optic, and elasto-optic tensors of $BaTiO_3$. *Phys. Rev. B* **50**, 5941–5949 (1994).
23. Evarestov, R. A. & Bandura, A. V. First-principles calculations on the four phases of $BaTiO_3$. *J. Comput. Chem.* **33**, 1123–1130 (2012).
24. Tang, P., Towner, D. J., Hamano, T., Meier, A. L. & Wessels, B. W. Electrooptic modulation up to 40 GHz in a barium titanate thin film waveguide modulator. *Opt. Express* **12**, 5962–5967 (2004).
25. Carpenter, R. O. 'B. The electro-optic effect in uniaxial crystals of the dihydrogen phosphate type III. Measurement of coefficients. *J. Opt. Soc. Am.* **40**, 225–229 (1950)..
26. Bernasconi, P., Zgonik, M. & Günter, P. Temperature dependence and dispersion of electro-optic and elasto–optic effect in perovskite crystals. *J. Appl. Phys.* **78**, 2651–2658 (1995).
27. DiDomenico, M. & Wemple, S. H. Oxygen–octahedra ferroelectrics. I. Theory of electro–optical and nonlinear optical effects. *J. Appl. Phys.* **40**, 720–734 (1969).
28. Veithen, M. & Ghosez, P. Temperature dependence of the electro-optic tensor and refractive indices of $BaTiO_3$. *Phys. Rev. B* **71**, 132101 (2005).
29. Kvasov, A. et al. Piezoelectric enhancement under negative pressure. *Nat. Commun.* **7**, 12136 (2016).
30. Shirane, G., Pepinsky, R. & Frazer, B. C. X-ray and neutron diffraction study of ferroelectric $PbTiO_3$. *Acta Crystallogr.* **9**, 131–140 (1956).
31. *Materials Handbook: A Concise Desktop Reference* (Springer International Publishing, Cham, Switzerland 2018).
32. Schafranek, R. et al. $PbTiO_3/SrTiO_3$ interface: energy band alignment and its relation to the limits of Fermi level variation. *Phys. Rev. B* **84**, 045317 (2011).
33. Železný, V. et al. The variation of $PbTiO_3$ bandgap at ferroelectric phase transition. *J. Phys. Condens. Matter* **28**, 025501 (2016).